Article

Lightweight, Passive Radiative Cooling to Enhance Concentrating Photovoltaics

No Radiative Cooling

Low Thermal Radiation

Apply Radiative Cooling

With Radiative Cooling

Extra Thermal Radiation

Solar Power = 6.1 W

Solar Power = 6.1 W

T_{PV} 36°C   27 %

V_{OC}

- Coolers
- Solar Cell
- Enclosure
- Fresnel Lens
- Heat Sink
- Enclosure

T_{PV} = 110 °C
V_{OC} = 0.27 V

T_{PV} = 74 °C
V_{OC} = 0.34 V

— Cooler
— Heat Sink
— Cooler
— Substrate
— Solar Cell

Concentrating Photovoltaics Setup   **Radiative Cooling Assembly**

Ze Wang, David Kortge, Jie Zhu, Zhiguang Zhou, Hans Torsina, Changkyun Lee, Peter Bermel

pbermel@purdue.edu

HIGHLIGHTS

Radiative cooling for CPV is a cheap, lightweight add-on requiring no power

A 36°C temperature drop is achieved, leading to a 31% increase of V_{OC}

A 4 to 15 times extension of lifetimes for various CPV cells is predicted

Different cooling structures are investigated at a wide range of conditions

Concentrating photovoltaics (CPV) experience higher heat loads from focused sunlight, requiring careful thermal management. Often, active cooling is required that increases costs and reduces net power production. By applying the cheap, passive, and lightweight radiative cooling mechanism on top of the traditional cooling approaches, we experimentally demonstrate a temperature drop of 36°C for CPV, leading to a 31% increase of open-circuit voltage for GaSb cell and 4 to 15 times predicted lifetime extension.

Article

Lightweight, Passive Radiative Cooling to Enhance Concentrating Photovoltaics

Ze Wang,[1] David Kortge,[1] Jie Zhu,[1] Zhiguang Zhou,[1] Hans Torsina,[2] Changkyun Lee,[2] and Peter Bermel[1,2,3,*]

SUMMARY

Radiative cooling can reject significantly more waste heat than convection and conduction at high temperatures by sending it directly into space. As a passive and compact cooling mechanism, radiative cooling is lightweight and does not consume energy. These qualities are promising for thermal management in outdoor systems generating low grade heat, such as concentrating photovoltaics (CPV) and thermophotovoltaics (TPV). In this work, we first simulate radiative cooling for a wide range of working conditions, including heat loads from 6 to 100 W with different CPV cooling designs. We then demonstrate a CPV system integrated with radiative coolers, achieving a 5°C to 36°C temperature drop and an 8% to 27% relative increase of open-circuit voltage for a GaSb solar cell, under a heat load of above 6 W with different cooling designs. We show that the temperature drops from radiative cooling may significantly improve CPV system lifetimes.

INTRODUCTION

Thermal management is extremely important for renewable energy systems, such as photovoltaics (PV), thermophotovoltaics (TPV), and concentrating photovoltaics (CPV). Elevated operating temperatures not only reduce the efficiency of PV modules,[1] but also substantially reduce their lifetimes.[2–4] This is an even more critical issue for higher heat load systems, such as TPV and CPV, where low-band-gap solar cells are commonly used, making the system more sensitive to temperature increases. The encapsulated housing of CPV and TPV systems further suppresses convective cooling, leading to dramatic temperature rises.

Heat transfer methods potentially relevant to CPV and TPV systems are conduction, convection, and radiation.[5] Conventional PV cooling approaches usually only utilize convective or conductive heat transfer, such as heat sinks, convective or forced air cooling, liquid cooling, etc. Some of these strategies require extra energy input and specially designed cooling systems, which can increase the cost and reduce the overall reliability. Radiative cooling, on the other hand, had been overlooked until recently. Although it is limited for most of the indoor and low-temperature applications, as the temperature difference between the object and ambient is not large enough to fully exploit its potential, radiative cooling becomes powerful for outdoor applications, such as thermal management for buildings and PV systems. This difference is a result of direct access to atmosphere transparency window from 8 to 13 μm. Photons with wavelengths in this range can go through the atmosphere and exchange heat directly with outer space at a temperature around 3 K.[6] This large temperature difference enables outdoor radiative coolers to reject a great deal of waste heat.

Context & Scale

Concentrating photovoltaics (CPV) aim to focus sunlight on solar cells to improve efficiency and reduce material costs. However, concentration also increases heating of the solar cells, potentially offsetting efficiency improvements and reducing system lifetimes. Active cooling, such as forced air and liquid cooling, is usually required, but increases the cost while reducing net power production. Radiative cooling, on the other hand, uses thermal radiation to dissipate heat, which is cheap, lightweight, and requires no extra power. This is especially beneficial for enclosed CPV systems using solar trackers. Our experiment shows that by coupling radiative coolers on a flat heat sink, the solar cell operating temperature in a passively cooled CPV can be reduced by 36°C under a heat load of 6.1 W. As a result, a 27% relative increase of open-circuit voltage is observed for the GaSb cell. A lifetime extension of 4 to 15 times for typical CPV cells is also projected.
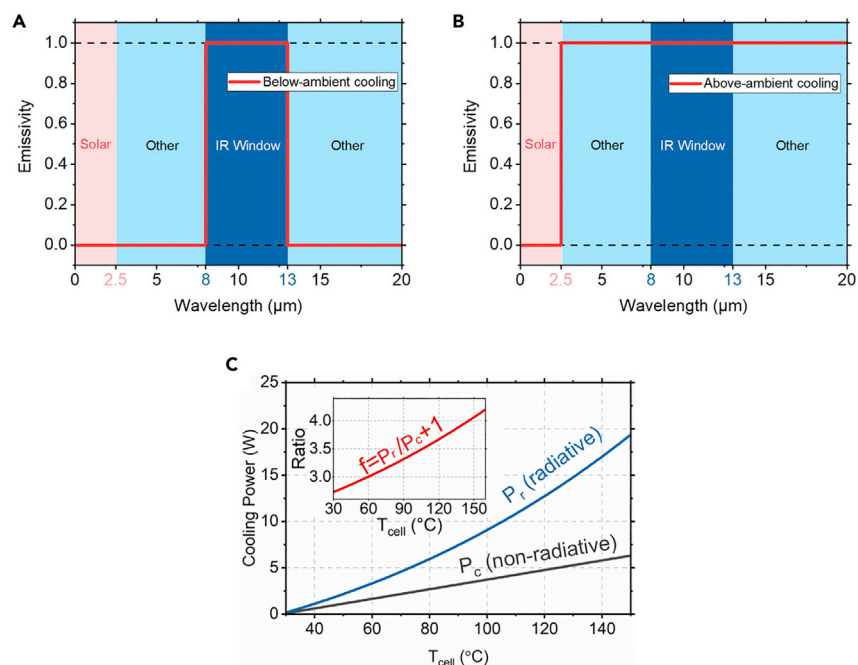
Figure 1. Emissivities of Two Types of Radiative Cooler and Cooling Performance for Thermal Management

(A) Ideal below-ambient cooler with unity emissivity in transparency window and zero elsewhere, which is suitable for buildings in order to achieve a low steady-state temperature.

(B) Ideal above-ambient cooler with zero emissivity in solar spectrum and unity elsewhere, which is suitable for PV systems to produce high cooling power.

(C) A comparison of cooling power provided by radiative cooling and non-radiative cooling approaches. The ambient temperature, non-radiative cooling coefficient, and emissivity are assumed to be 28°C, 3 W/m²/K, and 0.83, respectively. The inset shows cooling power enhancement of thermal radiation growing very fast as temperature increases, based on Equation 2, giving a 1.5 to 3 times higher cooling power than non-radiative cooling.

Radiative cooling can be classified as either below-ambient cooling or above-ambient cooling, as shown in Figures 1A and 1B. Below-ambient cooling aims for low steady-state temperatures, ideally to use a cooler with unity emissivity in the transparency window and zero elsewhere. However, the cooling power is limited due to the narrow radiation spectrum range. Above-ambient cooling, on the other hand, aims to provide a maximum cooling power, which ideally requires the cooler to absorb no power within the solar spectrum and emit as a blackbody at longer wavelengths.

A wide range of materials and structures have been demonstrated to provide radiative cooling.[7–9] In early work, nighttime below-ambient cooling was studied, as it does not require suppression of emission within the solar wavelengths. At this stage, bulk and composite materials with strong emissivity in transparency window were investigated intensively.[10–20] Daytime below-ambient cooling was not achieved until very recently, due to the challenges of simultaneously producing both strong infrared (IR) emittance and low solar absorption. The emergence of nanophotonic and metamaterial coolers has now made it possible to tailor the emittance spectrum more precisely than has been achieved with traditional bulk materials. Much stronger and flatter emittance plateaus in the atmospheric transmission window have now been achieved while suppressing solar absorption, enabling net cooling even under direct sunlight.[21–30] Meanwhile, above-ambient cooling with broadband IR

[1]Birck Nanotechnology Center, Purdue University, 1205 W. State St., W. Lafayette, IN 47907, USA

[2]School of Electrical and Computer Engineering, Purdue University, 501 Northwestern Ave., W. Lafayette, IN 47907, USA

[3]Lead Contact

*Correspondence: pbermel@purdue.edu

https://doi.org/10.1016/j.joule.2020.10.004

emittance has also been proposed and studied recently,[24,26,29,31–33] which can provide a great deal of cooling for objects at high temperatures. Moreover, a recent study showed that given a proper design, broadband coolers can also be used for below-ambient cooling, since the thermal heat exchange with the sky outside of the transparency window can provide additional cooling power at near-ambient temperatures.[30]

Different types of radiative cooling can be used, depending on the working temperature of the system. For example, below-ambient cooling is widely used for thermal management of buildings,[9,34–37] while above-ambient radiative cooling is more suitable for dissipating low grade heat from PV systems,[24,26,31–33] as the elevated working temperature and high sky transmittance create ideal conditions for maximizing the cooling power. Unlike forced air or liquid cooling for PV systems, which consume 2% to 5% of the total output power,[38,39] radiative cooling is passive with no extra energy consumption.[40] It is also compact, lightweight, and reliable, without any bulky heat sinks or moving parts, as in air or liquid cooling. This aspect can benefit PV or CPV modules integrated with tracking systems. More importantly, the radiative power is significantly larger and grows quickly at high temperatures. Its rate of heat dissipation is proportional to the fourth power of the temperature difference of the two objects,[5] which scales much faster than conduction and convection. The efficient, compact, and passive nature of radiative cooling makes it an outstanding cooling mechanism for PV systems.

Recent research has shown the effects of radiative cooling in PV, TPV, and CPV systems.[24,26,31–33] Last year, a GaSb-based CPV system with soda-lime radiative cooler was experimentally demonstrated. A 10°C drop of the solar cell was achieved under 13 suns, leading to a relative increase of 5.7% in open-circuit voltage and an estimated 40% increase in lifetime.[33]

In this work, we studied the radiative cooling performance of CPV in three different cooling structures, under a range of wind speeds and solar heat loads. We also conducted multiple outdoor experiments covering the worst and best possible working scenarios for radiative cooling to check the overall performance. The experiments showed that radiative cooling, depending on the working conditions, can contribute roughly 25% to 62% of the overall cooling power of a CPV system equipped with flat-plate heat sink, while adding little weight and no extra power consumption. A high-concentration PV system integrated with radiative cooling was designed, refined, and fabricated based on our previous study.[33] The average heat load on the solar cell in our experiment was ~5 to 6 W. By applying two soda-lime radiative coolers on both sides of the heat sink, the temperature drop of GaSb cell at steady state for worst and best cases were 5°C and 36°C, respectively. To our knowledge, the maximum temperature drop even outperformed some active air cooling methods.[39,40] The temperature decrease also resulted in a 8% to 27% (28 to 75 mV) relative (absolute) increase in the open-circuit voltage of our GaSb PV cell, as well as a projected lifetime extension for various types of solar cells, which potentially can be used in CPV systems.[41–45] Using detailed simulations, a peak radiative power flux of 157 to 310 W/m^2 was estimated to be present, thereby increasing the cooling performance per unit weight by 25% to 81%. This improvement is particularly beneficial to PV systems with solar trackers. To better illustrate the concept, we define the specific cooling power S_p to be:

$$S_p = \frac{P_r + P_c}{m(T_{cell} - T_a)}, \qquad \text{(Equation 1)}$$

where P_r and P_c are the radiative and non-radiative cooling power, respectively; m is the total weight of the entire cooling assembly; T_{cell} is the solar cell temperature; and T_a is the ambient temperature.

For cooling systems working at the same temperature, a higher S_p indicates a greater cooling power per unit weight. By integrating radiative cooling into the CPV, the S_p increase can be calculated as a ratio factor f, which is given by:

$$f = \frac{S_{p,r}}{S_{p,c}} \approx \frac{(P_r + P_c)}{P_c} = \frac{\sigma \varepsilon \left(T_{cell}^4 - T_a^4\right)}{h_{eff}\left(T_{cell} - T_a\right)} + 1, \qquad \text{(Equation 2)}$$

where $S_{p,r}$ and $S_{p,c}$ are the specific cooling power of our assembly with and without radiative cooling, respectively; h_{eff} is the effective coefficient for non-radiative heat transfer; σ is the Stefan–Boltzmann constant; and ε is emissivity of the cooler. The approximation can be made as long as the coolers are much lighter than the remainder of the cooling assembly, and the operating temperatures remain the same. It is straightforward to show that $f \sim T_{cell}^3$ when T_{cell} is large, which implies that radiative cooling is more resilient to high temperature systems than other cooling methods. Figure 1C gives a better interpretation of the specific cooling power improvement. As temperature goes up, the radiative cooling power grows to quickly dominate the total cooling power, providing a substantially larger S_p. The total cooling power must match the heating power reaching the PV system under thermal steady state. Thus, with radiative cooling, PV can work under higher solar concentrations at the same temperature, to potentially improve efficiencies and power outputs.

In the remainder of this paper, we explore how a CPV demonstration setup has been built to achieve the desired metrics of radiative cooling enhancement in a lightweight form factor, and how this design benefits both the operating open circuit voltage as well as long-term reliability. After presenting our experimental methodology, we show our key experimental results, as well as simulations to validate our understanding and interpretation. We then extend this framework to consider coolers that can perform even better for commercial CPV systems at higher heat loads from 6 to 100 W, corresponding to ~100% to 1600% of the input solar heat demonstrated in our setup. Different cooling designs are also simulated with quantitative data to provide a comprehensive understanding of radiative cooling performance under a wide range of convective heat transfer conditions. Finally, we conclude by summarizing the key results in this work and discuss potential directions for future research.

RESULTS

The radiative cooling measurement platform consists of three chambers, as illustrated in Figure 2D. Each chamber is designed for different functions. Chamber 1, as shown in Figure 2A, contains a solar cell and two soda-lime glass radiative coolers, while Chamber 2 has a similar structure without any coolers. Instead, aluminum (Al) reflectors are used in Chamber 2 as a control to minimize the solar heating and suppress the temperature, which is common for cooling outdoor devices under direct sunlight. The top low-density polyethylene (LDPE) films in both chambers can be attached or removed to represent different working conditions. The sealed-chamber structure (with top LDPE) can serve as a reference for two different scenarios. First, it roughly represents the zero wind speed working condition of CPV (natural convection), since the LDPE film can cut off direct convection from the heat sink to ambient air. Second, it can be compared with active air-cooled CPV at zero air-injection rate, since many actively cooled CPV systems require an enclosed fluid channel.[39] In either case, the sealed-chamber structure gives the highest possible temperature drop from radiative cooling. On the other hand, the open-
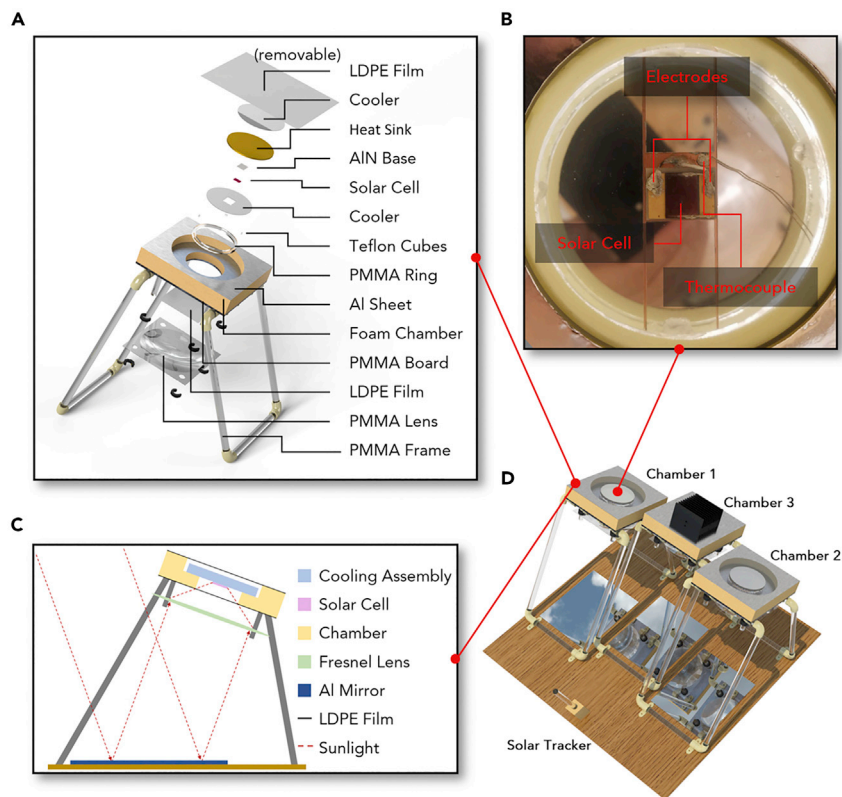
Figure 2. Experimental CPV Setup to Measure the Performance of Radiative Cooling

(A) A rendered, exploded view of Chamber 1, with each component labeled on the side.

(B) A photograph of the electrodes and thermocouple connecting to the solar cell on the bottom of Chamber 1.

(C) A sketch tracing solar rays into the chambers, with no details shown inside the chamber.

(D) A rendered picture of the entire CPV setup (excluding the tripod, cables, and data logging equipment).

chamber structure (without top LDPE) is best compared to passively air-cooled CPV, which is widely used in commercial CPV. Both structures are tested outdoors and show considerable temperature drops. Electrode probes and type-K thermocouples are mounted to the solar cells in Chambers 1 and 2 to measure their open-circuit voltages (V_{OC}) and temperatures (T_{expt}), as shown in Figure 2B. Chamber 3 only has a thermal power sensor to monitor the incident solar power. All three chambers are equipped with a Fresnel lens with effective diameter of 6 inches. Considering the zenith angle of sunlight at our field test location, all chambers are tilted at 20°C and fixed on a wood board to maintain the same orientation, which orients the top cooler horizontally during experiments to maximize its view factor to the sky. The wood board is held by a tripod, the tilt and azimuth angles can be adjusted to track the sun. Three first-surface Al mirrors are placed on the board under each chamber separately to reflect sunlight normally to the polymethyl methracylate (PMMA) Fresnel lens, as shown in Figures 2C and 2D. A PMMA rod is fixed in front and tilted 20°C to serve as a solar tracker. Further details are provided in Experimental Producessures section.

Daytime Radiative Cooling Field Test

A daytime outdoor cooling experiment was conducted on September 14, 2019, as shown in Figure 3. LDPE covered both chambers during the experiment. The site had open access to the sky to guarantee the expected cooling performance, as
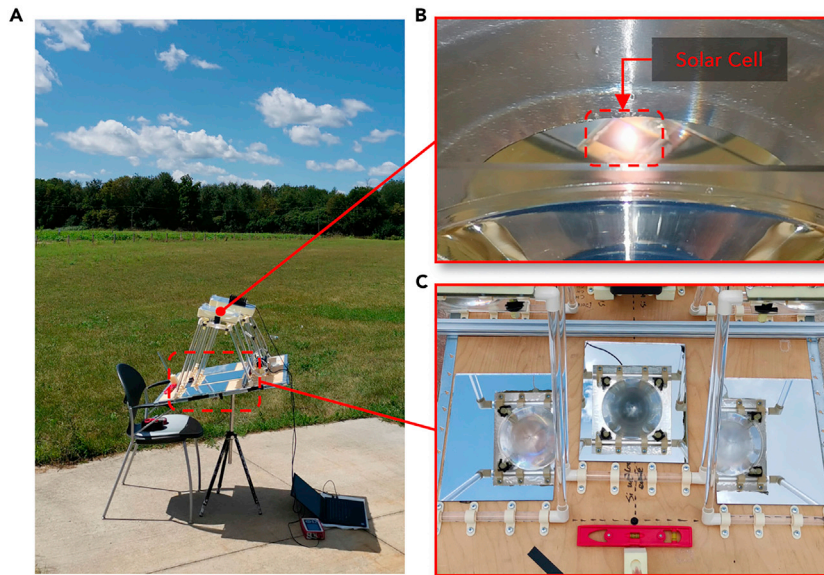
**Figure 3. Photos Taken During the Outdoor Field Test**
(A) A photo showing the experimental environment. The cooler in the setup has open access to the sky.
(B) A photo showing the focused beam spot falling on the center of the solar cell.
(C) A zoomed-in photograph, showing the reflection of the three chambers through the Al mirrors.

shown in Figure 3A. The role that each of the three chambers played in the experiment is described in the Results section, above. Before the test, all three chambers were aligned to the same level and warmed up by exposing to direct sunlight for 30 min, to reach a steady-state temperature close to ambient. During the test, the tilt and azimuth angles of the setup were manually adjusted approximately every 5 min to focus the beam spot on the center of the solar cells, as shown in Figures 3B and 3C. The temperature T_{expt} and open circuit voltage V_{OC} of solar cells for both Chamber 1 and Chamber 2 were measured at resolutions of 0.096°C and 0.12 mV, respectively, with a 2 Hz sampling rate. The thermal power meter in Chamber 3 monitored the input solar irradiance at a rate of 1 Hz. A laboratory chair and a tripod were used to stabilize the setup against vibrations caused by the wind. The experiment lasts for at least 1.5 h to ensure that both chambers reach an instantaneous thermal steady state.

The measured real-time solar cell temperatures T_{expt}, as well as a simulation of this experiment, are shown in Figure 4A. The shaded areas of the simulated temperatures account for the errors caused by uncertainties (see Table S3) in the solar power meter measurements in Chamber 3. The experimental data and simulation results exhibited a very good match to the level of uncertainty, suggesting that the model may reflect the most important physical effects on the instantaneous thermal steady state of the system. The real-time V_{OC} values for the solar cells in the two chambers are shown in Figure 4B. With the Fresnel lens, the average focused solar irradiance during experiment was measured to be around 6.1 W, corresponding to a direct normal irradiance (DNI) of 1,019 W/m². It can be seen in the figures that the differences between chambers of both T_{expt} and V_{OC} values are smallest at the beginning of the experiment, since both chambers start at similar, above-ambient temperatures caused by solar heating during the 30-min warm-up phase. Upon direct solar heating, temperatures rose significantly in both chambers, thus reducing V_{OC} for
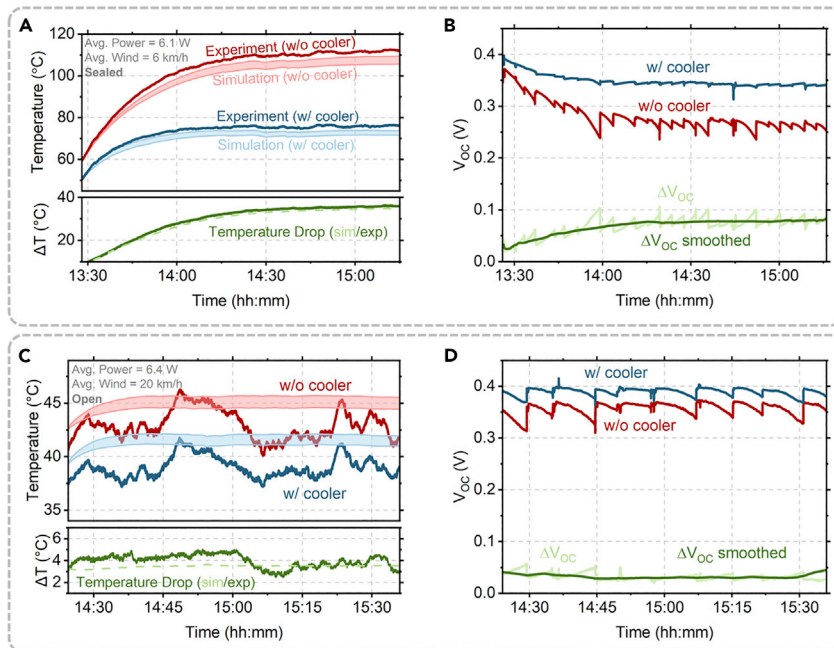
Figure 4. Experimental and Simulation Data for Daytime Radiative Cooling

Measured (solid lines) and simulated (shaded areas and dashed line) temperatures of solar cells in Chamber 1 (w/ cooler) and Chamber 2 (w/o cooler) are plotted together to show the radiative cooling performance. The range of each shaded area reflects experimental uncertainties in the solar power measurement. The open-circuit voltage V_{OC} of solar cells in both chambers are shown next to the corresponding temperature result.

(A) Temperature result for experiment conducted on September 14, 2019. Average solar power input, wind speed, and chamber structure are noted in the top-left corner. Temperature drops are plotted in the bottom sub-figure.

(B) Measured open-circuit voltage V_{OC} of solar cells on September 14, 2019. The difference of ΔV_{OC} is calculated, smoothed, and shown for clarity. Sharp jumps are caused by manual tracking.

(C) Temperature results for experiment conducted on September 4, 2020. Hourly wind speed data used in the simulation does not track transient wind gusts to precisely simulate the temperatures, but the averages match closely.

(D) Measured open-circuit voltage V_{OC} of solar cells on September 4, 2020 shows a consistent difference of at least 28 mV.

both cells at different rates. More specifically, the temperature of Chamber 1 (with coolers) increased more slowly than the temperature of Chamber 2 (without coolers), as expected. Given that the structures and environments of the two chambers were nearly identical, except for the presence of the radiative coolers, the temperature differences observed are attributed to their additional cooling power. The V_{OC} of Chamber 1 also dropped more slowly than that of Chamber 2, which implies higher electric power generation. The zigzag curves of the V_{OC} were caused by manual solar tracking, where each small jump corresponded to regular micro-adjustments of the tilt and azimuth angles with respect to the sun. This behavior is not observed in Figure 4A, because the heat capacity of the system is relatively significant. This caused the temperature of the cooling assembly to respond to the beam spot shifts with a time constant on the order of 1 min. It can also be noticed that the V_{OC} increased in Chamber 1 at each jump but decreased in Chamber 2. This divergence in behavior was likely caused by the different local absorptance of the two cells, as well as the slightly different patterns of focused beam spots. This means the reduced energies on both solar cells were not identical, even if the shifted distances of the spots were the same during each adjustment. Both chambers reached instantaneous thermal

Table 1. Key Simulation Results for Outdoor Field Tests on September 14, 2019 (sealed chamber) and September 4, 2020 (open chamber)

Steady-State Solution	Notation	Sealed Chamber		Open Chamber	
		Chamber 1	Chamber 2	Chamber 1	Chamber 2
Solar cell temperature	T_{cell} [°C]	73.9	110.5	38.8	42.7
Cooling power per unit area (up)	$P_{r,up}/A_{cooler,up}$ [W/m²]	309.5	37.8	157.2	10.9
Cooling power per unit area (down)	$P_{r,down}/A_{cooler,down}$ [W/m²]	169.6	28.0	45.1	4.9
Total radiative cooling power	P_r [W]	3.6	0.5	1.6	0.13
Total input power	P_{in} [W]	5.9	5.8	6.4	6.3
Direct convective coefficient	h_{air} [W/m²/K]	–	–	28.5	28.5
Effective convective coefficient	h_{eff} [W/m²/K]	2.8	3.7	19.1	19.3
Specific cooling power	S_p [W/kg/K]	0.49	0.27	1.62	1.30

steady state at roughly 14:30. The temperature drop caused by the coolers was 36°C at their peak values, which even outperformed some active air cooling but required no energy consumption.[39] This significant temperature decrease led to a higher open-circuit voltage around 75 mV, corresponding to a 27% relative increase (since the shifts of V_{OC} are different in the two chambers, only the highest 10% of V_{OC} readings from each chamber are considered to provide a fair comparison, for when the beam spots are well focused on both).

To investigate radiative cooling in the more challenging case of high convection, a similar daytime outdoor cooling experiment without a top LDPE film installed was conducted on September 4, 2020, a windy day (wind speed at 20 km/h). The results can be seen in Figures 4C and 4D. As expected, temperatures in both chambers were lower than the sealed-chamber case because of increased convection. Fluctuations in Figure 4C are greater than in Figure 4A, as the heat sink is now much more sensitive to wind gusts. While hourly wind speed data used in simulations missed fluctuations from wind gusts, the average temperature matched experiments closely. The measured temperature drop in Chamber 1 was ~3°C to 5°C under an average wind speed of 20 km/h (previously, it was only 6 km/h). Simulations showed that wind speed increases raised the effective convective heat transfer coefficient of the heat sink inside chamber from ~3 to 20 W/m²/K. Although the temperature drop is not as high as the sealed-chamber case, the open-circuit voltage in Chamber 1 (with cooler) is still ~28 mV greater than Chamber 2 (without cooler), as shown in Figure 4D, corresponding to an 8% relative increase.

More experiments were conducted on different days to cover a wider range of heat loads and convective heat transfer coefficients. The heat transfer uniformity of Chambers 1 and 2, as well as the electrical characteristics of GaSb solar cells in both chambers, have also been tested in separate experiments and show a very close performance. These additional experimental and simulation results can be found in Tables S2 and S5; Figure S2–S3.

Quantitative Simulation Analysis
The experiments described in the prior section were also simulated. Key results are shown in Table 1. For the sealed-chamber case, the net cooling power of the top soda-lime glass

cooler and the Al reflector were found to be ~310 and ~38 W/m²/K, respectively. The power provided by the cooler was almost one order of magnitude greater than that given by the Al reflector. Although the bottom cooler and the Al reflector did not face the sky, the cooling power from cooler was still significantly higher than provided by the Al reflector. Thus, both the top and bottom coolers contributed a large amount of cooling power, providing ~62% of the total. This also illustrates that radiative cooling can still provide considerable cooling power for above-ambient applications, even without direct sky access. The effective convective coefficient h_{eff} for the assembly disk (including top, bottom, and side surface areas) was 2.8 W/m²/K in Chamber 1 and 3.7 W/m²/K in Chamber 2 (see Equation S3). The higher convective coefficient in Chamber 2 was caused by higher buoyancy-driven convection, induced by higher operating temperatures. Moreover, due to the compactness and high cooling flux of radiative cooling, the specific cooling power S_p of the assembly disk was greatly improved, as illustrated in Equation 1. In our setup, the S_p in Chamber 1 was 0.49 W/kg/K, as a result of both radiative and convective cooling; while in Chamber 2, the S_p was only 0.27 W/kg/K without radiative cooling. Simply by applying two layers of soda-lime glass wafers, the S_p can increase by 81% without any extra energy input in a sealed-chamber structure. For the open-chamber case, despite a lower temperature drop, the radiative cooling power from coolers still greatly exceeded that of Al reflectors, contributing ~25% of the total cooling power, with net values of 157.2 and 10.9 W/m² from the top surfaces, respectively. Direct access to ambient air increased the effective convective coefficients h_{eff} of the cooling assembly disks to 19.1 and 19.3 W/m²/K, respectively; whereas, the convective coefficient h_{air} of the top surface in direct contact with ambient air was 28.5 W/m²/K for both chambers. As a reference, for outdoor experiments with the open chamber, the typical value of h_{eff} was approximately 10 W/m²/K (see Table S2). The unusually high h_{eff} caused a lower temperature drop in the open-chamber experiment at only ~4°C. Simulations showed that the temperature drop should reach around 10°C if under the same weather as the sealed-chamber experiment. Also, because of the additional cooling power from radiative coolers, S_p rose from 1.30 to 1.62 W/kg/K (~25% relative improvement). Combined, these two experiments show the most extreme cases for radiative cooling, where the h_{eff} ranges from the lowest to highest possible values for our CPV setup. In most other conditions, radiative cooling provides a temperature drop between these two values (see Table S2).

The performance of CPV radiative cooling can vary significantly with the choice of cooling design and working environment. For example, the radiative cooling power usually increases when the heat load becomes larger and becomes less obvious when the convective coefficient is higher. Therefore, choice of heat sink, wind speed, and heat load all affect performance. With a better cooling design, greater heat loads can be accepted by the solar cell to improve the overall efficiency and output power. To acquire a comprehensive understanding of radiative cooling, three groups of simulations are carried out to study the performance and upper limit of multiple CPV cooling designs at 28°C under various heat loads and wind speeds, including a flat-plate heat sink in sealed chamber (with top LDPE film), a flat-plate heat sink in open air (without top LDPE film), and a finned heat sink in open air (without top LDPE film). The geometries of the first two groups are the same as shown in Figure 2A, while the heat sink in the third group is replaced with a finned heat sink to achieve the greatest convective cooling power (see Figure S5 for details). The maximum allowed operating temperature of solar cell is assumed to be ~110°C. The result is shown in Figure 5A. The top and bottom lines in each of the three groups indicate working environments with wind speeds of 0 (natural convection) and 6 km/h, respectively. Lower wind speeds reduce convective cooling, resulting in a higher heat sink temperature and increased radiative cooling power for a
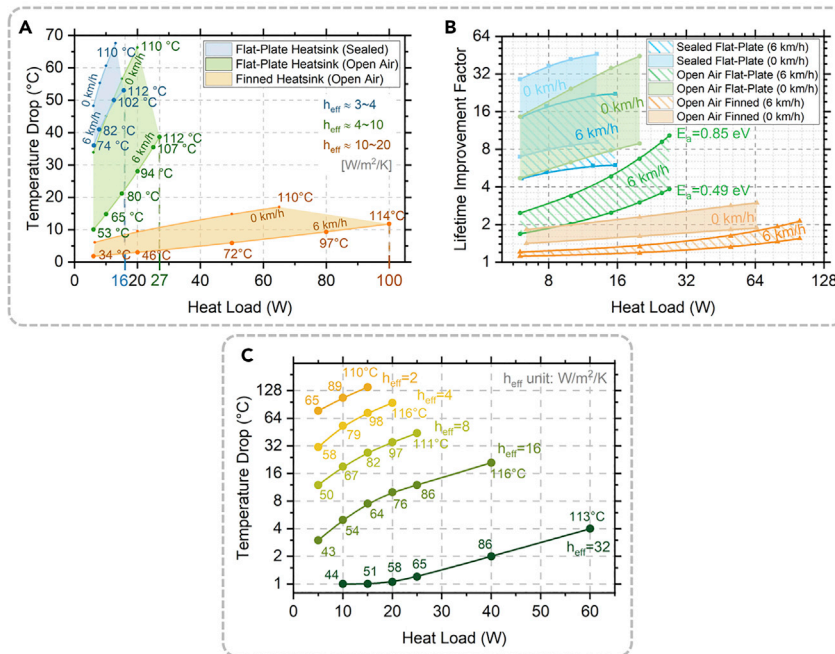
Figure 5. Simulations of Various CPV Cooling Designs under a Wide Range of Working Conditions at 28°C Ambient

(A) Possible solar cell temperature drops for a range of heat loads and wind speeds using three different radiative cooler designs: flat-plate heat sink in sealed chamber (blue area), flat-plate heat sink in open air (green area), and finned heat sink in open air (orange area). The round dots indicate the simulation data points, and solid lines indicate the interpolated temperature drops of the corresponding cooling designs. Each group has a top and bottom line, indicating the cases of wind speed at 0 or 6 km/h, respectively. The corresponding temperatures of solar cells equipped with radiative coolers are noted next to the data points. For readability, only bottom lines are noted (see Figure S5 for details). The maximum heat load for each group is noted on the x axis, illustrating the limitation of radiative cooling with the corresponding cooling design. Once above this value, the temperature of the solar cell will rise beyond ~110°C, which is impractical for CPV applications. The estimated convective heat transfer coefficient h_{eff} for each group is noted with the corresponding color.

(B) Lifetime improvement factors correspond to the three groups shown in the left figure with the same color. The x and y axis are logarithmic ($\log_2$) to show a wider range. Each line from the left figure becomes an area in this figure. The top and bottom lines in each area show the lifetime improvement at activation energies of 0.85 and 0.49 eV, respectively. Shaded and lined areas indicate the cases of wind speeds at 0 and 6 km/h, respectively.

(C) Temperature drops from radiative cooling under different convective coefficients h_{eff} and heat loads. Each line with different color represents a group of simulation at a certain h_{eff} as noted. Data points are the simulated temperature drops, whereas the lines are interpolated drops. The temperature of Chamber 1 (w/ cooler) for each data point is noted with the corresponding color, similar as the above figure.

larger temperature difference. Convective cooling is very sensitive to wind speed, while radiative cooling is not directly affected by wind, making it benefit all designs and perform best in a low wind speed environment. As shown in the blue region, radiative cooling on a flat-plate heat sink in a sealed-chamber cooling structure can provide a huge temperature drop without active air cooling. However, the maximum heat load of this design is the lowest: ~13 W (zero wind) and ~16 W (wind speed at 6 km/h), respectively. When using a flat-plate heatsink in fully open air (top LDPE removed), as illustrated in the green area, radiative cooling can still provide a significant temperature drop, giving a maximum heat load of ~20 W (zero wind) and ~27 W (wind speed at 6 km/h). This group of simulations has a

cooling structure and convective coefficient most similar to commercial CPV designs. Finally, for high-heat-load CPV systems equipped with finned heat sinks, radiative cooling can only lower the temperature by 3°C to 6°C with a 20 W heat load. However, the temperature drop can increase to 12°C to 13°C when the heat load is above 65 W, which can further increase the maximum heat load of the CPV setup by ~15 to 18 W compared with the non-radiative cooling design. Although the temperature drop is lower than the other two cases, the improvement to the maximum heat load from radiative cooling is the highest for the finned heat sink structure.

To summarize the radiative cooling performance under different working conditions, the temperature drop versus heat load and h_{eff} was simulated using a flat-plate geometry. Figure 5C shows the temperature drop due to radiative cooling at different values of h_{eff}; similar to Figure 5A, where the plot is grouped by the cooling design. As before, the corresponding temperature of Chamber 1 (with cooler) was noted by the side of each data point. Given the verified accuracy of the model from multiple experiments, these results can guide researchers exploring different CPV cooling designs.

Lower operating temperatures also dramatically improve the lifetime of most solar cells, including commercially available products. In general, solar cells can be modeled to degrade over time following the Arrhenius rate equation.[45] Depending on the material, type, and fabrication quality of the PV module, the degradation rate can vary dramatically as a result of variations in the failure mechanisms and the associated activation energy E_a. Since many different types of solar cells are used in CPV systems, including III-V, multi-junction, and high-performance silicon (Si) solar cells, the following discussion will encompass these possibilities, instead of just focusing on the GaSb solar cell used in the CPV setup. For most Si solar cells, E_a usually falls in the range from 0.7 to 0.9 eV.[42] Activation energies for other materials are taken from different references,[43–45] at a range from 0.49 to 0.85 eV. Using temperature data from the experiments and simulations, the lifetime improvements by radiative cooling for each line shown in Figure 5A are estimated in Figure 5B. As can be seen, with different types of PV panels at an activation energy from 0.49 to 0.85 eV, each line from Figure 5A expands to an area. Specifically, for the experiment conducted on September 14, 2019, a 4 to 13 times extension of lifetime is predicted (lined blue area). Similarly, roughly 0.7 to 1.5 (70% to 150%) times extension (lined green area) for an open-chamber structure is predicted, at a heat load and wind speed of 6 W and 6 km/h. For the finned heat sink, at a wind speed of 6 km/h (lined orange area), the minimum lifetime extension from radiative cooling is 10% to 20%. By checking the data points of interest, Figures 5A–5C can be used as look-up tables to predict the temperature drop and improvement for solar cell lifetime resulted from radiative cooling.

DISCUSSION

In this work, a GaSb CPV system integrating soda-lime glass-based radiative coolers was demonstrated and tested in outdoor experiments. The cooling performance was quantitatively modeled by an opto-thermal simulation, which showed a good match with experimental data. Three different cooling designs (flat-plate heat sink in sealed chamber, flat-plate heat sink in open chamber, and finned heat sink in open chamber) were investigated and quantitatively analyzed. Depending on the cooling design, heat load, and wind speed, radiative cooling performance can vary to a large extent. For flat-plate heat sinks in sealed chambers, a large temperature drop of 36°C is achieved experimentally at a heat load of 6.1 W (DNI = 1,019 W/m², wind speed = 6 km/h), with a 75 mV increase of V_{OC} (27% relative). A total cooling power of 310 and

170 W/m^2 from the top and bottom coolers, respectively, is estimated, representing 62% of the overall cooling power; furthermore, the cooling power per unit weight of the assembly disk is increased by 81%. This overall temperature reduction from radiative cooling is comparable to some active air-cooling systems yet requires no extra power input. For this cooling design, the maximum heat load is limited to ∼16 W without active cooling. The second cooling structure uses the same flat-plate heat sink but operates in open air to fully take advantage of natural convection. However, no active-air cooling system can be applied beyond the open-chamber structure. A temperature drop over 5°C is achieved in outdoor tests, under a heat load of 6.4 W (DNI = 1,069 W/m^2, wind speed = 20 km/h), resulting in a V_{OC} increase of 28 mV (8% relative). The radiation power from top and bottom coolers is 157 and 45 W/m^2, respectively, contributing to 25% of the total cooling power, which improves the specific cooling power by 25%. Three groups of simulations were conducted to further study radiative cooling performance under heat loads from 6 to 100 W, with different wind speeds and cooling designs. The results clearly show that radiative cooling benefits all cases, despite variations in heat sinks and weather conditions. While the temperature drop from radiative cooling becomes less obvious with better convective cooling, the absolute increase of maximum heat load improves (from flat-plat heat sink to finned heat sink). Lifetime extensions from the reduced operating temperatures for the corresponding designs are predicted for different types of solar cells, which may be used in similar CPV systems; if confirmed, this would provide substantially improved reliability for the entire CPV system. Figures 5A and 5C summarize the radiative cooling performance for these designs by demonstrating the relationship between heat load, convective coefficients, and temperature drop. Finally, the radiative cooling approach presented here is not limited to CPV, but can be applied to substantially enhance passive cooling for a wide range of applications, which generate low grade heat and operate above ambient temperatures. The materials for radiative cooling are not limited to the soda-lime glass structures demonstrated in this work. Many cooling approaches, including active cooling, can be coupled with radiative coolers and provide greater cooling power, by changing the surface emissivity of the heat sink or enclosure of the device. We hope that this work can help to motivate further studies on commercially relevant CPV cooling designs, as well as other systems, which may benefit from radiative cooling.

EXPERIMENTAL PROCEDURES

Resource Availability

Lead Contact

Further information and requests for resources and materials should be directed to and will be fulfilled by the Lead Contact, Peter Bermel (pbermel@purdue.edu).

Materials Availability

This study did not generate new unique materials.

Data and Code Availability

The COMSOL simulation file and MATLAB code generated during this study are available upon request to the corresponding author.

Daytime Radiative Cooling Experiment

The detailed structure of Chamber 1 is shown in Figure 2A. The outside enclosure is made of polystyrene (PS) foam covered by Al sheets to minimize the absorption of sunlight. The enclosure protects the assembly from various weather conditions and reduces noise in the collected data. Two highly transparent LDPE films are used to seal the openings on the top and the bottom of the chamber, respectively, to suppress convection and any associated temperature fluctuations caused by wind gusts. LDPE films and the foam

housing are included to partially resemble the enclosed working environment seen in commercial CPV systems. Most commercial CPV systems in real application have enclosures similar to our CPV setup, without a large amount of direct natural convection. By placing or removing the top LDPE film, radiative cooling performance can be studied under different working conditions. Additionally, although having a low thermal conductivity, the foam housing will not strongly hinder the cooling of the inside structure, since the heat convection mainly dissipates vertically through LDPE films. Simulations show that there is only a 10% relative increase of the effective convection coefficient associated with replacing the foam with a 0.05-inch-thick copper enclosure (see Figure S4C; Table S4), which is comparable to a commercial CPV system. Inside the chamber, the solar cell, aluminum nitride (AlN), copper heat sink and coolers were pasted together as a cooling assembly disk at diameter of 4 inches by thermally conductive silver adhesive, to uniformly conduct heat from solar cell to coolers. The inner side of the coolers were coated with 300 nm Al as a reflection layer. Four Teflon cubes and a PMMA ring were used to elevate the disk to limit the conductive heat transfer from the disk to the chamber walls, protecting the foam from high temperatures. The electrode probes were connected to the solar cells to measure the corresponding open-circuit voltage (V_{OC}). A Type-K thermocouple was mounted next to the solar cell on the disk with silver adhesive to measure the temperature (T_{expt}), as shown in Figure 2B. The data were collected by a four-channel USB DAQ to record the V_{OC} and T_{expt}.

Chamber 2 had almost an identical structure as Chamber 1, but the coolers were replaced with Al reflectors as a control. The Al is commonly used as a solar reflector to minimize solar heating of devices under direct sunlight because of its light weight, reasonable cost, and widespread availability. Therefore, among non-radiative cooling materials, Al is one of the best choices for suppressing the temperature of outdoor systems.

Chamber 3 had the same enclosure as Chamber 1 and 2, while the inside assembly was replaced with a thermal power sensor (S314C, Thorlabs). A meter console (PM100D, Thorlabs) was connected to the sensor to measure the focused solar power. Chamber 2 and 3 were not shown here separately due to their similarities (for more information, please see Table S1; Figure S1; Video S1).

The reflectance and transmittance of the first-surface Al mirror, PMMA lens, and LDPE films are shown in Figure 6A. The high values in the solar spectrum range ensure a minimal optical loss for the CPV setup. The spectrum DNI data of West Lafayette extracted from National Solar Radiation Database (NSRDB) is also shown in the same figure for reference. The emissivities of the Al reflector and cooler are shown in Figure 6B. The transmittance of the clear sky, extracted from the MODTRAN mid-latitude summer sky model,[46] is shown for reference. Both the Al reflector and cooler have a low emittance from 0.3 to 4 μm, minimizing the heating caused by sunlight. Above 4 μm, the high conductivity of Al gives a low mid-IR emittance, trapping heat inside the assembly disk. On the contrary, the emittance of the radiative cooler rises quickly above 5 μm, which provides a significant output cooling power in the mid-IR. All data in both figures from 0.3 to 2.5 μm were measured by spectrophotometer (Lambda-950, PerkinElmer); data above 2.5 μm for the cooler were measured on an FTIR (Nexus 670).[33]

Simulation Analysis of the Experiment
Simulations were carried out with COMSOL Multiphysics[47] to quantitatively analyze the cooling performance and verify the experimental results. The transient heat
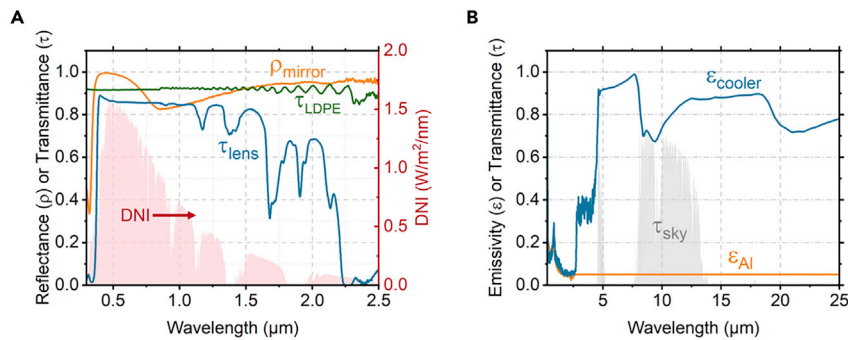
Figure 6. Key Parameters of the CPV Setup

(A) Reflectance and transmittance of the first-surface Al mirror, PMMA lens, and LDPE film. The DNI is shown for reference. The transmittance and reflectance of mirror, lens, and LDPE film are relatively high within the solar spectrum, to reduce the optical loss.

(B) Emissivities of the Al-coated soda-lime glass cooler and the Al reflector. The sky transmittance is shown for reference. The cooler has a high emissivity in the atmospheric transparency window to maximize the cooling power, while Al has a much lower value.

transfer process was modeled in software and matched well with experiment, as previously shown in Figure 4A.

To ensure the accuracy of simulation results, a geometry reflecting the real configuration of the setup was necessary. To improve the efficiency, an axisymmetric structure was used as an approximation of the real structure. As seen in Figure 7, several modifications have been made. The solar cell, the AlN base, and the bottom cooler were replaced with three disks with equal surface areas and thicknesses, correspondingly, to keep the total conducted heat same. The foam wall of the chamber was adjusted to a round structure, with the same average wall thickness as in the experiment. The holder elevating the chamber was neglected, since the heat was mostly dissipated through the walls. The simplified axisymmetric geometry was verified to have a very similar performance as the original configuration in terms of heat transfer, yet it gave a much faster calculation speed (see Figures S4A and S4B). Therefore, an axisymmetric geometry was used for quantitative simulation analysis in this work. More details are introduced in supplemental material (see Figures S6–S9; Tables S6–S7).

The model includes heat transfer, laminar air flow, and thermal radiation to reflect the real physical processes taking place, ensuring the reliability of the results. Material properties, including the density, thermal conductivity, heat capacity, were extracted from manufacturer's data sheets and online database. The surface emissivity for each material was measured on the Lambda 950 spectrophotometer and the FTIR spectrometer. The boundary conditions, including solar irradiance, wind speed, humidity, ambient temperature, were defined based on the experimentally measured solar power and the local weather reports, to faithfully reflect real-world experimental conditions.
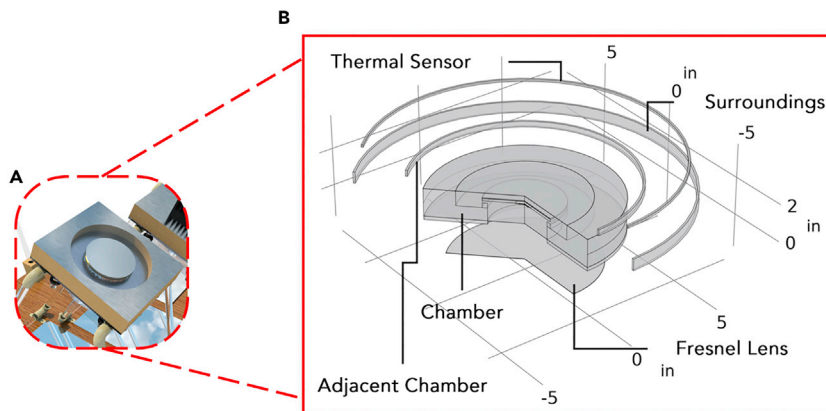
Figure 7. Simulation Geometry of Chamber 2

(A) Real geometry of the chamber.

(B) Simplified axisymmetric geometry used in simulation. The three rings surrounding the chamber server as radiation surfaces of adjacent chamber wall, thermal sensor, and surrounding buildings and trees, which block part of the view from chamber to sky. The heights and diameters are calculated such that the view factors from top cooler to the rings are roughly the same as real condition. The Fresnel lens at bottom is also included in the simulation as it blocks mid-IR thermal radiation.

AUTHOR CONTRIBUTIONS

Z.W., Z.Z., and P.B. conceived and designed the experiment. Z.W. and P.B. wrote and revised the manuscript. Z.W. and Z.Z. designed and fabricated the radiative cooling CPV setup. Z.W., J.Z., D.K., H.T., and C.L. conducted outdoor field tests. Z.W. performed data processing and simulations. H.T. and C.L. analyzed and verified the simulation results.

DECLARATION OF INTERESTS

The authors declare no competing interests.

REFERENCES

1. Dubey, S., Sarvaiya, J.N., and Seshadri, B. (2013). Temperature dependent photovoltaic (PV) efficiency and its effect on PV production in the world – a review. Energy Procedia 33, 311–321.

2. Sun, X., Silverman, T.J., Zhou, Z., Khan, M.R., Bermel, P., and Alam, M.A. (2017a). Optics-based approach to thermal management of photovoltaics: selective-spectral and radiative cooling. IEEE J. Photovoltaics 7, 566–574.

3. Han, Y., Meyer, S., Dkhissi, Y., Weber, K., Pringle, J.M., Bach, U., Spiccia, L., and Cheng, Y.-B. (2015). Degradation observations of encapsulated planar CH3NH3PbI3 perovskite solar cells at high temperatures and humidity. J. Mater. Chem. A 3, 8139–8147.

4. Espinet-González, P., Algora, C., Núñez, N., Orlando, V., Vázquez, M., Bautista, J., and Araki, K. (2015). Temperature accelerated life test on commercial concentrator III-V triple-junction solar cells and reliability analysis as a function of the operating temperature. Prog. Photovolt. Res. Appl. 23, 559–569.

5. Howell, J.R., and Siegel, R. (2002). Thermal Radiation Heat Transfer (Taylor and Francis).

6. Fixsen, D.J. (2009). The temperature of the cosmic microwave background. Astrophys. J. 707, 916–920.

7. Sun, X., Sun, Y., Zhou, Z., Alam, M.A., and Bermel, P. (2017b). Radiative sky cooling: fundamental physics, materials, structures, and applications. Nanophotonics 6, 997–1015.

8. Hossain, M.M., and Gu, M. (2016). Radiative cooling: principles, progress, and potentials. Adv. Sci. 3, 1500360.

9. Zeyghami, M., Goswami, D.Y., and Stefanakos, E. (2018). A review of clear sky radiative cooling developments and applications in renewable power systems and passive building cooling. Sol. Energy Mater. Sol. Cells 178, 115–128.

10. Catalanotti, S., Cuomo, V., Piro, G., Ruggi, D., Silvestrini, V., and Troise, G. (1975). The radiative cooling of selective surfaces. Sol. Energy 17, 83–89.

11. Bartoli, B., Catalanotti, S., Coluzzi, B., Cuomo, V., Silvestrini, V., and Troise, G. (1977). Nocturnal and diurnal performances of selective radiators. Appl. Energy 3, 267–286.

12. Granqvist, C.G., and Hjortsberg, A. (1981). Radiative cooling to low temperatures: general considerations and application to selectively emitting SiO films. J. Appl. Phys. 52, 4205–4220.

13. Granqvist, C.G., Hjortsberg, A., and Eriksson, T.S. (1982). Radiative cooling to low temperatures with selectivity IR-emitting surfaces. Thin Solid Films 90, 187–190.

14. Granqvist, C.G., and Hjortsberg, A. (1980). Surfaces for radiative cooling: silicon monoxide films on aluminum. Appl. Phys. Lett. 36, 139–141.

15. Eriksson, T.S., Jiang, S.-J., and Granqvist, C.G. (1985). Surface coatings for radiative cooling applications: silicon dioxide and silicon nitride made by reactive rf-sputtering. Sol. Energy Mater. 12, 319–325.

16. Diatezua, D.M., Thiry, P.A., Dereux, A., and Caudano, R. (1996). Silicon oxynitride multilayers as spectrally selective material for passive radiative cooling applications. Sol. Energy Mater. Sol. Cells 40, 253–259.

17. Kimball, B.A. (1985). Cooling performance and efficiency of night sky radiators. Sol. Energy 34, 19–33.

18. Orel, B., Gunde, M.K., and Krainer, A. (1993). Radiative cooling efficiency of white pigmented paints. Sol. Energy 50, 477–482.

19. Nilsson, T.M.J., Niklasson, G.A., and Granqvist, C.G. (1992). A solar reflecting material for radiative cooling applications: ZnS pigmented polyethylene. Sol. Energy Mater. Sol. Cells 28, 175–193.

20. Nilsson, T.M.J., and Niklasson, G.A. (1995). Radiative cooling during the day: simulations and experiments on pigmented polyethylene cover foils. Sol. Energy Mater. Sol. Cells 37, 93–118.

21. Yeng, Y.X., Ghebrebrhan, M., Bermel, P., Chan, W.R., Joannopoulos, J.D., Soljacic, M., and Celanovic, I. (2012). Enabling high-temperature nanophotonics for energy applications. Proc. Natl. Acad. Sci. USA 109, 2280–2285.

22. Rephaeli, E., Raman, A., and Fan, S. (2013). Ultrabroadband photonic structures to achieve high-performance daytime radiative cooling. Nano Lett. 13, 1457–1461.

23. Raman, A.P., Anoma, M.A., Zhu, L., Rephaeli, E., and Fan, S. (2014). Passive radiative cooling below ambient air temperature under direct sunlight. Nature 515, 540–544.

24. Zhu, L., Raman, A., Wang, K.X., Anoma, M.A., and Fan, S. (2014). Radiative cooling of solar cells. Optica 1, 32.

25. Chen, Z., Zhu, L., Raman, A., and Fan, S. (2016). Radiative cooling to deep sub-freezing temperatures through a 24-h day–night cycle. Nat. Commun. 7, 13729.

26. Zhu, L., Raman, A.P., and Fan, S. (2015). Radiative cooling of solar absorbers using a visibly transparent photonic crystal thermal blackbody. Proc. Natl. Acad. Sci. USA 112, 12282–12287, https://doi.org/10.1073/pnas.1509453112.

27. Zou, C., Ren, G., Hossain, M.M., Nirantar, S., Withayachumnankul, W., Ahmed, T., Bhaskaran, M., Sriram, S., Gu, M., and Fumeaux, C. (2017). Metal-loaded dielectric resonator metasurfaces for radiative cooling. Adv. Opt. Mater. 5, 1700460.

28. Zhai, Y., Ma, Y., David, S.N., Zhao, D., Lou, R., Tan, G., Yang, R., and Yin, X. (2017). Scalable-manufactured randomized glass-polymer hybrid metamaterial for daytime radiative cooling. Science 355, 1062–1066.

29. Kou, J.-L., Jurado, Z., Chen, Z., Fan, S., and Minnich, A.J. (2017). Daytime radiative cooling using Near-black infrared emitters. ACS Photonics 4, 626–630.

30. Xue, X., Qiu, M., Li, Y., Zhang, Q.M., Li, S., Yang, Z., Feng, C., Zhang, W., Dai, J.G., Lei, D., et al. (2020). Creating an eco-friendly building coating with smart subambient radiative cooling. Adv. Mater. e1906751.

31. Li, W., Shi, Y., Chen, K., Zhu, L., and Fan, S. (2017). A comprehensive photonic approach for solar cell cooling. ACS Photonics 4, 774–782.

32. Zhou, Z., Sun, X., and Bermel, P. (2016). Radiative cooling for thermophotovoltaic systems. Proc. SPIE 9973, Infrared Remote Sensing and Instrumentation XXIV. https://doi.org/10.1117/12.2236174.

33. Zhou, Z., Wang, Z., and Bermel, P. (2019). Radiative cooling for low-bandgap photovoltaics under concentrated sunlight. Opt. Express 27, A404–A418.

34. Goldstein, E.A., Raman, A.P., and Fan, S. (2017). Sub-ambient non-evaporative fluid cooling with the sky. Nat. Energy 2, 9.

35. Al-Obaidi, K.M., Ismail, M., and Abdul Rahman, A.M.A. (2014). Passive cooling techniques through reflective and radiative roofs in tropical houses in Southeast Asia: a literature review. Front. Archit. Res. 3, 283–297.

36. Gentle, A.R., and Smith, G.B. (2015). A subambient open roof surface under the mid-summer sun. Adv. Sci. 2, 1500119.

37. Sadineni, S.B., Madala, S., and Boehm, R.F. (2011). Passive building energy savings: a review of building envelope components. Renew. Sustain. Energy Rev. 15, 3617–3631.

38. Wang, S., Shi, J., Chen, H.-H., Schafer, S.R., Munir, M., Stecker, G., Pan, W., Lee, J.-J., and Chen, C.-L. (2017). Cooling design and evaluation for photovoltaic cells within constrained space in a CPV/CSP hybrid solar system. Appl. Therm. Eng. 110, 369–381.

39. Xiao, M., Tang, L., Zhang, X., Lun, I., and Yuan, Y. (2018). A review on recent development of cooling technologies for concentrated photovoltaics (CPV) systems. Energies 11, 3416.

40. Du, D., Darkwa, J., and Kokogiannakis, G. (2013). Thermal management systems for Photovoltaics (PV) installations: a critical review. Sol. Energy 97, 238–254.

41. Ndiaye, A., Charki, A., Kobi, A., Kébé, C.M.F., Ndiaye, P.A., and Sambou, V. (2013). Degradations of silicon photovoltaic modules: a literature review. Sol. Energy 96, 140–151.

42. Luo, W., Khoo, Y.S., Hacke, P., Naumann, V., Lausch, D., Harvey, S.P., Singh, J.P., Chai, J., Wang, Y., Aberle, A.G., and Ramakrishna, S. (2017). Potential-induced degradation in photovoltaic modules: a critical review. Energy Environ. Sci. 10, 43–68.

43. Park, N.C., Oh, W.W., and Kim, D.H. (2013). Effect of temperature and humidity on the degradation rate of multicrystalline silicon photovoltaic module. Int. J. Photoenergy 2013, 1–9.

44. Hoffmann, S., and Köhl, M. (2012). Effect of humidity and temperature on the potential-induced degradation. Prog. Photovolt. Res. Appl. 22, 173–179.

45. Hacke, P., Spataru, S., Terwilliger, K., Perrin, G., Glick, S., Kurtz, S., and Wohlgemuth, J. (2015). Accelerated testing and modeling of potential-induced degradation as a function of temperature and relative humidity. IEEE J. Photovoltaics 5, 1549–1553.

46. Berk, A., Bernstein, L.S., Anderson, G.P., Acharya, P.K., Robertson, D.C., Chetwynd, J.H., and Adler-Golden, S.M. (1998). MODTRAN cloud and multiple scattering upgrades with application to AVIRIS. Remote Sens. Environ. 65, 367–375.

47. Pryor, R.W. (2009). Multiphysics modeling using COMSOL®: a first principles approach (Jones & Bartlett Publishers).